

## The Canadian Automated Meteor Observatory (CAMO): System overview

R.J. Weryk<sup>a,\*</sup>, M.D. Campbell-Brown<sup>a,b</sup>, P.A. Wiegert<sup>a,b</sup>, P.G. Brown<sup>a,b</sup>, Z. Krzeminski<sup>a</sup>, R. Musci<sup>a</sup>

<sup>a</sup> Dept. of Physics and Astronomy, Univ. of Western Ontario, London, Canada N6A 3K7

<sup>b</sup> Centre for Planetary Science and Exploration, UWO, London, Canada N6A 5B7

### ARTICLE INFO

#### Article history:

Received 18 September 2012

Revised 10 January 2013

Accepted 19 April 2013

Available online 3 May 2013

#### Keywords:

Meteors

Image processing

Data reduction techniques

Photometry

### ABSTRACT

We describe the hardware and software for the Canadian Automated Meteor Observatory (CAMO), an automated two-station video meteor system designed to facilitate simultaneous radar-video meteor detections, to help constrain numerical ablation models with higher precision meteor data, and to measure the meteoroid mass influx at the Earth. A guided system with a wide-field ( $\sim 30^\circ$ ) camera detects meteors ( $<+5^M$ ) and positions an optical scanner such that a narrow-field ( $\sim 1^\circ$ ) camera tracks the meteors in real-time. This allows for higher precision deceleration measurements than traditionally available, and for detailed studies of meteoroid fragmentation. A second system with a wide-field ( $\sim 20^\circ$ ) camera detects fainter ( $<+7^M$ ) meteors (in non-real-time) primarily for meteoroid mass influx measurements. We describe the system architecture, automation control, and instruments of CAMO, and show example detections. We find narrow-field trajectory solutions have precisions in speed of a few tenths of a percent, and radiant precisions of  $\sim 0.01^\circ$ . Our initial survey shows 75% of all tracked, multi-station meteor events ( $<+5^M$ ) show evidence of fragmentation, either as discrete fragments (17% of total), or in the form of meteor wake. Our automatic wide-field camera solutions have average radiant errors of  $\sim 3^\circ$  and speed uncertainties of 3%.

© 2013 Elsevier Inc. All rights reserved.

## 1. Introduction

### 1.1. Motivation and importance

Video observations of meteors allow for the determination of the physical properties of meteoroids. These properties, such as mass and bulk/grain density, rely on astrometric and photometric measurements and can be used to provide constraints for both numerical ablation and meteoroid stream models. When combined with simultaneous measurements from other instruments such as radar, system biases can be estimated. This ultimately leads to better understanding of the cometary and asteroidal parent objects of the associated meteoroids. Furthermore, if the ablation behaviour (single-body vs fragmenting, differential ablation, etc.) of individual meteoroids can be documented in detail, it may allow for meteoroid compositions to be better understood, and perhaps answer questions such as whether chondrules exist in comets (Brownlee et al., 2012), their mass/size distributions, and Solar System origin.

Video meteor observations can be either fully automated, partially automated, or non-automated. Fully automated systems require no user intervention for automation control, event detection, or automated reduction analysis. Such systems are complex to build, but are highly desirable as they allow for data collec-

tion that otherwise might not be recorded. Partially automated systems may handle some of these tasks without user intervention, but may be as time consuming as non-automated systems. Manual review of events has the advantage of data quality control. Previous simultaneous radar-video measurements (Weryk and Brown, 2012, 2013) using the Canadian Meteor Orbit Radar (CMOR) and a number of Gen-III image-intensified CCD cameras had a limited dataset due to the difficulty in manually gathering observations, as the video meteor detection routines were only partially automated, with no automated analysis.

In this work, we describe an automated system developed to address the need for larger numbers of video meteor measurements, namely the Canadian Automated Meteor Observatory (CAMO), and show examples to demonstrate the capabilities of the system. One of the key goals of CAMO is to have an automated system to observe video meteors for comparison with their corresponding radar echoes observed by CMOR (Jones et al., 2005) and to use these simultaneous observations to better understand ablation behaviour, especially by constraining values of the luminous efficiency,  $\tau_l$ . This efficiency represents the fraction of kinetic energy loss converted into light, and must be known to determine meteor mass from video meteors. Additional goals of CAMO include:

1. Measuring meteor trail radii to help constrain the initial radar trail radius effect (Jones and Campbell-Brown, 2005).

\* Corresponding author.

E-mail address: [weryk@meteor.uwo.ca](mailto:weryk@meteor.uwo.ca) (R.J. Weryk).

2. Making higher spatial and temporal resolution studies of meteor wake and fragmentation.
3. Estimating meteor shower parameters and activity.
4. Measuring the meteoroid mass influx for both shower and sporadic sources.
5. Determining mass and velocity distributions.

In particular, higher precision measurements of meteor position as a function of time will lead to a better understanding of the micro-physical details of meteoroid ablation, and intrinsic meteoroid physical properties, such as the bulk and grain densities. This in turn provides insight into the material distribution in the Solar System.

### 1.2. Previous video studies

Previous camera networks using photographic film have concentrated on fireballs as opposed to the millimetre-sized meteoroid population (Hawkes, 2002) which is the focus of CAMO. Because CAMO is a video based system rather than photographic, the methods for meteor detection and analysis differ significantly.

There exist many video meteor networks, which typically use the detection software MeteorScan (Gural, 1997), MetRec (Molau, 1999), ASGARD (Weryk et al., 2008), or UFOCapture (SonotaCo, online). A common feature of most video networks is automatic event detection and some form of system automation, however, automatic analysis of events is less common. A review of analysis techniques for all forms of optical instruments may be found in Hawkes (2002).

CAMO is inspired by the AIM-IT system, described by Jenniskens et al. (2004) and Gural et al. (2004). AIM-IT was the first system to track meteors in real-time using an optical scanner system coupled to a narrow field instrument, with a wide field instrument guiding the scanner. Meteoroid fragmentation was visible in as many as 20% of detected meteors.

## 2. System specifications

CAMO consists of two nearly identical video stations. The first is co-located with CMOR near Tavistock, Ontario (43.264°N, 80.772°W, +324 m) while the second is located near Elginfield, Ontario (42.193°N, 81.316°W, +319 m), a separation of 44.9 km. All cameras are aimed northward to avoid direct illumination from the Moon. The guided system FOV overlap between the two stations is largest at 90 km height, while the influx system FOV overlap is largest at 105 km height. The CAMO system first ran in 2007, with automation implemented by 2009.

### 2.1. System hardware

Each CAMO station has two fully digital camera systems: a wide-field and narrow-field system, collectively named the “guided system”, and a second wide-field camera for mass influx measurements. The weather resistant enclosures of both systems are housed in the same shed under a computer controlled roll-off roof, illustrated in Fig. 1.

The hardware specifications for each system are listed in Table 1. Each system uses progressive scan digital CCD cameras lens-coupled to ITT NiteCam 380 Gen-III image intensifiers, which have ~60 line pairs per mm resolution. The two cameras (wide and narrow) of the guided system have independent frame rates up to 110 fps, while the influx system captures at 20 fps. All cameras connect via fibre-optic cable to EDT PCI DV frame-grabbers. The timebase is calibrated to UTC using GPS receivers and the Network Time Protocol (NTP) software. In our set up, NTP phase-locks the

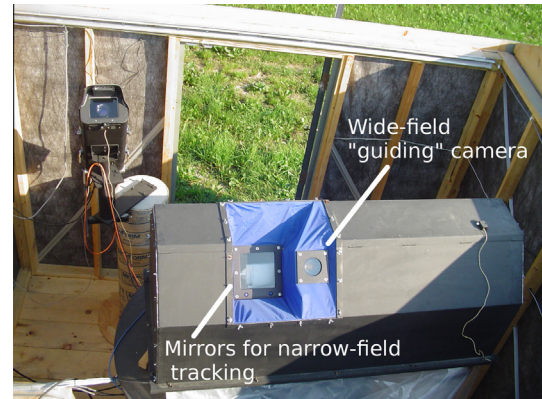


**Fig. 1.** Hardware layout of the influx and guided system under the roll-off roof shed. The influx system, shown in the top left, runs independent of the guided system, shown in the bottom right. A photo switch is pictured on top of the guided system enclosure, which disconnects power to the image-intensifiers during unwanted bright light.

**Table 1**

CAMO system specifications. The wide and narrow-field cameras of the guided systems are handled by the same control computer. The stellar and meteor magnitude limits are inversely proportional to camera frame rate. All cameras are digital progressive scan. The precision is measured perpendicular to the meteor trajectory.

System	Guided system (wide; narrow)	Influx system (wide)
Resolution	640 × 480	1600 × 1200
Frame rate	80 fps; 110 fps	20 fps
Bit-depth	12-bit	14-bit
Stellar limit	+7.5 <sup>M</sup> ; ~+7 <sup>M</sup>	+8.5 <sup>M</sup>
Meteor limit	+5.5 <sup>M</sup> ; <+5 <sup>M</sup>	+6.5 <sup>M</sup>
Detection software	ASGARD	MeteorScan
Camera	Imperx IPX-VGA120L	Cooke PCO.1600
Optics	25 mm f/0.85; 545 mm f/11	50 mm f/0.95
Intensifier	18 mm GaAs Gen-III	25 mm GaAs Gen-III
FOV size	28°; 1.5°	20°
Precision	76 m; 4 m @ 100 km	22 m @ 100 km

system clock to the PPS (pulse per second) output of a Garmin 18× LVC GPS receiver, giving an estimated absolute time accuracy of ~10 μs. However, the relative frame-to-frame timing error per meteor is negligible. The cameras are in weather resistant enclosures, with the optics behind BK-7 optical glass. The protective glass in front of the guided wide-field camera has a parallelism of ≤15', while it is ≤5" for the other two cameras. The guided system uses a UEI PD2-AO-8/16 PCI digital-to-analogue card to control a two-axis Cambridge Technology 6900 optical scanner (Cambridge Technology, online) which positions a set of mirrors to track meteors in real-time (as will be discussed in Section 3.4). This scanner can slew at 2000 deg/s over a 40° × 40° region with a small angle response time of 6.0 ms, a short term position repeatability of 0.3", and a zero-drift stability of 2.0"/°C.

The narrow-field camera and its image-intensifier connect to a William Optics Zenithstar 80 II ED APO f/6.8 refractor telescope which gathers light reflected by the optical scanner mirrors. However, the size of the mirror surfaces reduces the aperture from 80 mm to 50 mm giving an effective focal ratio of f/11 for our guided narrow-field camera. While this is much smaller than our f/0.85 guided wide-field camera, there is correspondingly less sky background per pixel. Note that this aperture value is for an object centred on the optical scanner axis. Detections imaged off-axis have less aperture for the narrow-field camera, and therefore, larger *f*-stops. The effective limiting magnitude for meteors is brighter than the stellar limit, as the light from a meteor is spread out across many pixels. The layout of the guided system is shown in Fig. 2.

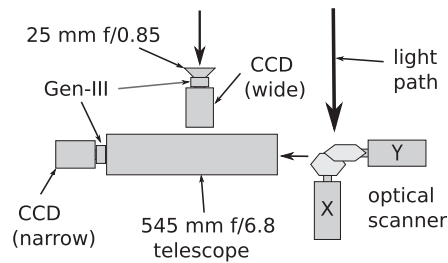


**Fig. 2.** Optical layout of the guided system in its weather resistant enclosure. The optical scanner directs light through a refractor telescope, and is imaged by the narrow-field camera. The wide-field camera gathers light separately, and both cameras use Gen-III image intensifiers.

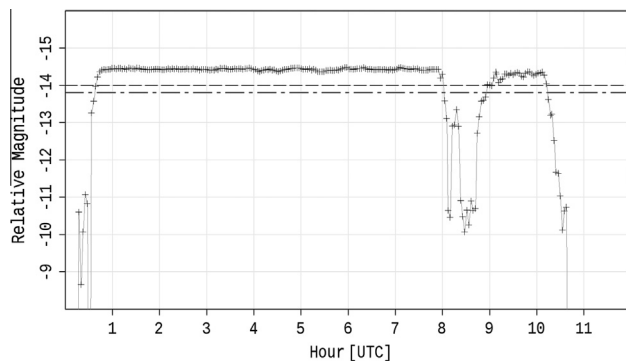


**Fig. 3.** An example of a nightly cloud detection record from the Polaris camera data, as measured on April 12, 2012. The upper threshold ( $-14.0^M$ ) is where conditions are considered favourable. When the relative magnitude drops below the lower threshold ( $-13.8^M$ ), the system stops operation. The fall off before 01:00 UTC represents sunset, while the fall off after 10:00 UTC represents sunrise. The decrease after 08:00 UTC represents a period of cloud.

Our Gen-III image-intensifiers have tube lifetimes of  $10^4$  h which will last over 5 years if used constantly, 5 h per night. Given the historical on-time statistics at our observing sites in Ontario, Canada, our tubes are expected to last more than 15 years. An intensifier tube lifetime is defined as the expected time until the gain decreases to half its initial factory value, corresponding to an instrumental magnitude change of  $0.75^M$ .

## 2.2. System automation

CAMO features full run-time automation using a separate control computer. This system uses a number of criteria to determine if conditions are appropriate for observation, such as the angular position of the Sun and Moon, local precipitation, outdoor temperature, and cloud coverage determined from a separate camera pointed towards Polaris. For this Polaris camera, 10 s of video frames from a 30 fps interlace-scan camera with a  $5^\circ$  FOV are averaged, Polaris located, and an uncalibrated instrumental magnitude measured. When this relative magnitude exceeds an empirically determined limit, cloud conditions are favourable. Polaris' magnitude is remeasured every 10 s. An example night of Polaris measurements is shown in Fig. 3. In addition, the per-frame background intensity from the Polaris camera is used as an indicator of sky brightness. Weather conditions are measured using a Davis Vantage Pro 2 model 6152 weather station. While the Moon must be below the horizon during normal system operation, this condition may be disabled during specialised campaigns.

When all the criteria shown in Table 2 are fulfilled, conditions are regarded as being favourable and the system enters its start phase. An in-house built power control interface powers a garage

**Table 2**

Automation modules used to determine if conditions are suitable for automatic data collection. The system does not run if the outside temperature is below a minimum value, due to mechanical issues with the roll-off roof during very cold temperatures. Separate start and stop conditions are needed to avoid ongoing starts or stops when one of the criterion fluctuates close to the trigger value.

Automation condition	Start	Stop
Precipitation	=0	>0
Wind speed	$\leq 50$ km/h	>50 km/h
Guided enclosure temp.	$>+7.0$ °C	$<+5.0$ °C
Outside temperature	$>-10.0$ °C	$<-12.0$ °C
Sun elevation angle	$<-13.5^\circ$	$>-13.5^\circ$
Moon elevation angle	$<-1.0^\circ$	$>-1.0^\circ$
Polaris relative magnitude	$<-14.0^M$	$>-13.8^M$
Polaris background light	<34	>37

door opener which opens the roll-off roof that covers the weather resistant enclosures. The cameras and optical scanner are supplied with power, and each system is instructed to perform its camera initialisation. Lastly, the detection/recording software is instructed to run and the image-intensifiers are powered on. This entire process takes less than 1 min. The system stops when any of the criteria in Table 2 are no longer satisfied. The stop sequence is to turn off the image-intensifiers, stop the detection/recording software, power down the cameras and optical scanner, and lastly close the roll-off roof. A web-based summary shows the system status, logs of weather conditions and cloud cover, and is updated every 5 min.

## 3. Detection and analysis

### 3.1. Meteor detection

The wide-field and narrow-field cameras of the guided system use the All-Sky and Guided Automatic Real-time Detection (ASGARD) software first described by Weryk et al. (2008). ASGARD provides real-time detection on the wide-field images (used to guide the narrow-field tracking), and has modular detection plugins. For all-sky meteor detection (Weryk et al., 2008) as used by the SOMN and NASA networks, a fixed-threshold module is used. For image-intensified video, the module accounts for dynamic noise on a per-pixel basis with the average pixel and noise levels determined from low-pass filters. These update on a per-frame basis and filter out frequencies above a set cut-off. Our approach is based on the general difference equation for an impulse response filter:

$$\sum_{j=0}^J a_j y_{n-j} = \sum_{k=0}^K b_k x_{n-k} \quad (1)$$

where  $J$  and  $K$  are the feed back and feed forward filter orders respectively, and  $a_j$  and  $b_k$  are weighting coefficients. It can be shown that a normalised first-order infinite impulse response low-pass filter is given by:

$$y_n = x_n + (y_{n-1} - x_n) \exp(-2\pi f_c / f_s) \quad (2)$$

where for a given pixel at frame  $n$ ,  $x_n$  is the pixel intensity,  $y_n$  is the filter value, and  $y_{n-1}$  is the filter value from the previous frame. The sampling frequency (i.e. frame rate) of the wide-field camera is  $f_s$ , and the cut-off frequency,  $f_c$ , relates to the time constant  $\tau = 1/2\pi f_c$ . This attenuates  $y_n$  to  $\exp(-1)$  in time  $\tau$  if  $x_n = 0$ . Our cameras are dominated by image-intensifier impulsive shot-noise, which is high frequency and easily filtered with this low-pass filter. To estimate the background noise for triggering purposes, a second filter uses  $x_n - y_{n-1}$  as input to dynamically set the threshold per pixel per frame. In practice, we find  $f_c = 0.2$  Hz for both the average and

noise filters is adequate for our wide-field camera under typical conditions.

To detect a meteor, the software loops over each pixel, and those pixels which exceed their average filter value by a configured threshold are counted in accumulation buffers corresponding to  $8 \times 8$  pixel tiles. When the count in any tile is  $\geq 6$  (i.e. six or more of the 64 pixels in the tile are above the configured threshold), the location is checked against a list of detections from previous frames. If no previous detections occurred in the same spatial region (within 16 pixels), a new detection is added to the list. A circular region (16 pixels in radius) centered on the trigger pixel in the image is then masked to prevent neighbouring pixels (presumed to be of the same event) from being detected as a duplicate event. Our implementation allows multiple events in the same video frame to be detected, such as when aircraft or satellites (which have longer dwell times) pass through the FOV, which would otherwise preclude the detection of meteors occurring at the same time. Events are removed from the detection list when they have not been linked to an earlier detection for 10 consecutive frames. Events lasting  $<4$  total frames are discarded. This may introduce an event duration bias, but we note it eliminates many false triggers.

For a pixel threshold of  $5.0\sigma$  above the background noise, manual inspection of 6.5 h of raw video data suggests the ASgard detection efficiency (the percentage of all real meteors that are detected) is 67%. This can be increased to 90% by lowering the threshold to  $2.5\sigma$ , however, doing so will tend to decrease the percentage of well tracked meteors as discussed in Section 3.4. We prioritise well tracked meteors rather than complete detection of every meteor for the guided system, and use a threshold of  $5.5\sigma$  during normal system operation. With this threshold, we typically detect up to 100 meteors per night when no major shower is active.

The influx system is used for meteoroid flux measurements, and uses MeteorScan (Gural, 1997) for non-real-time meteor detection. In tests, we find the detection efficiency is  $\sim 95\%$  for meteors  $<+5^M$ . Operationally, the recorded video is split into 10 min segments, which are processed by separate computing nodes via a Network File System (NFS). This allows the processing to complete before the next observing run, as 1 h of video requires 1.5 h of CPU time to process. Because this system produces data which requires manual reduction (using the methods of Weryk and Brown (2012, 2013)) to obtain velocities and light curves, we do not discuss it further, except to note that an example of its usage may be found in Musci et al. (2012).

### 3.2. Camera calibration

Measurements for the wide-field guided system are periodically calibrated manually using stars visible in calibration images, which are 10 s (800 frame) stack averages saved every 30 min during normal system operation. Using average stacks results in larger signal-to-noise ratio (SNR) compared to single frame images. We use the methods of Weryk and Brown (2012, 2013) for both astrometric and photometric calibration.

The astrometry is calibrated using the stellar positions from the SKY2000v4 catalogue (Myers et al., 2002), which have precisions of  $0.8''$ . We correct for stellar proper motion, precession, and nutation, to the local epoch. We use the azimuthal orthographic projection fit of Weryk and Brown (2012), which uses two third order polynomials producing typical residuals of  $30''$  for the wide-field camera of the guided system. We find this method gives smaller fit residuals compared to a gnomonic projection fit.

The photometry is calibrated using the stellar *R*-band magnitudes from the SKY2000v4 catalogue (Myers et al., 2002), as this photometric response better matches the instrument response of our Gen-III image-intensifiers as compared to the *V*-band response

(Weryk and Brown, 2013). This catalogue contains  $\sim 3 \times 10^5$  stars brighter than  $+8^M$ , which is more than adequate for our wide-field camera. To measure instrumental stellar magnitudes, a circular aperture of four pixel radius is used to sum the light from individual stars. A circular ring between 8 and 12 pixel radii around each star is used to estimate the local background intensity for each star, which is subtracted from the aperture sum. Because our cameras have a linear response (i.e.  $\gamma = 1.0$ ), our photometric calibration is of the form:

$$M = -2.5 \log_{10} I + C \quad (3)$$

where the pixel intensity sum ( $I$ ) and stellar magnitude ( $M$ ) for all stars are combined in a least-squares fit to determine the calibration offset ( $C$ ). For Elginfield, our calibration was found to typically be  $-11.46^M \pm 0.05^M$ . We do not perform real-time flat-fielding for our automatic photometry, as most of the optical vignetting occurs beyond the FOV of our 1/3 inch CCDs.

### 3.3. Meteor measurement

Meteor positions are automatically measured in real-time using a centre-of-mass algorithm applied to individual frames using the pixels within a circular region around the pixel that triggered the detection. As this algorithm is sensitive to impulsive shot-noise generated by our intensifiers, we perform our centroid repeatedly in each frame, each iteration using a smaller radius than the previous. Currently, we use two iterations of 24 and 8 pixel radii. Centroiding in this manner may produce small systematic offsets in speed when compared to centroids measured near the leading edge of the meteor (Weryk and Brown, 2012). While Weryk and Brown (2012) showed that manual analysis of the same meteor by multiple users can result in differences in the per-frame fiducial picks of  $\sim 1$  pixel, our automated analysis is expected to have larger differences than manual picks. Additional complications that may affect the accuracy of centroid picks are fading light curves, scintillation of stars near a meteor, and meteor wake. If significant amounts of wake become visible in the wide-field camera, an artificial deceleration may be introduced.

To measure an instrumental meteor magnitude, our software (in real-time) sums all pixel intensities within a circular aperture of 8 pixel radius. This radius is larger than the circular aperture used for stellar calibration because meteors are more extended. The per-pixel background intensity from the average filter (see Section 3.1) is subtracted, and the intensity sum is converted to a calibrated apparent magnitude using Eq. (3). While a meteor may occasionally saturate either the Gen-III image-intensifier or the CCD camera, our cameras are 12-bit which minimises this effect.

### 3.4. Mirror tracking

The idea of tracking a moving target using an optical scanner is not new. The first implementation for meteor tracking was the AIM-IT system described by Gural et al. (2004), which formed the early inspiration for development of the CAMO mirror-tracking camera. That system had a narrow-field interlace-scan camera with a  $6^\circ$  FOV that recorded every second frame (15 fps). Our narrow-field camera has a  $1.5^\circ$  FOV with a 110 fps progressive scan camera leading to better resolvability of the micro-physical ablation behaviour of meteors.

Calibration of the optical scanner system is performed manually, and is a multi-stage process. Because the  $1.5^\circ$  FOV contains at most a few visible stars, the scanner is stepped across the sky by increments of  $1.0^\circ$ . At each step, the camera acquires 24 frames which are averaged together. This stack is then rotated, scaled, and combined into a large mosaic image. Star identification between this mosaic image and the wide-field camera is performed manu-

ally, and the hardware encoder pointing of the optical scanner is adjusted until each target star is centred in the narrow-field camera FOV. This gives a high accuracy link between the wide field pixel centroid and the mirror encoder values. An affine plate mapping is generated between the wide-field pixel location, and the 16-bit hardware encoder values of the optical scanner, typically using at least 10 stars.

Once a meteor has been detected, it is tracked via the optical scanner system. Wide-field pixel locations are converted to hardware pointing units using the previously described affine mapping calibration (referred to as the guide plate). We use a fine-track algorithm, which steps the mirrors at high rate ( $\geq 2000$  steps per second) to track at the angular rate of motion of the meteor. This reduces meteor smearing and allows for individual fragments to be more easily resolved. However, extra latency is required at first detection to allow for measurement of the angular rate of the meteor. This initial slew rate is maintained until 3 s after the detection has ended in the wide-field camera. This allows meteors to be tracked beyond the edge of the wide-field FOV. As visible stars are smeared out using this fine-track algorithm, position measurements in the narrow-field must be reversed mapped back to their wide-field equivalents using the affine plate mapping, and then converted to zenith and azimuth angles using the astrometric plate mapping.

Image intensifier noise “blobs” and satellites pose a challenge to real-time guided meteor detection, as only one event can be tracked concurrently with the optical scanner. While non-real-time detection systems can reject false alarms during subsequent data review, our detection routines must be more stringent to reduce the number of missed tracked meteors that occurred while the optical scanner was tracking a non-meteor event. To eliminate most false alarms, we keep our detection threshold set higher (as discussed in Section 3.1) at  $5.5\sigma$  above the background noise and require events to last at least seven frames before being tracked. We use 80 fps for the wide-field camera during normal system operation, giving a track latency of  $\sim 90$  ms. Increasing the wide-field camera frame rate will decrease the track latency, however, doing so can negatively affect the astrometric centroid accuracy due to shorter exposure time frames being affected more by the impulsive noise generated by our image-intensifiers.

### 3.5. Multi-station meteor correlation

Each station independently copies text summaries of its events to a central server via the Internet. These summaries include the time, centroid location, and magnitude for the meteor in each frame. Our correlation program groups events from both stations based on the time of the brightest frame, using a 5 s overlap window. Event trajectories are computed automatically using the program MILIG (Borovička, 1990) and events having valid trajectories are written to a summary table. We define an event to be a valid multi-station meteor detection if the speed is  $>6$  km/s, the end height is between 10 and 200 km, with a begin height above 40 km, but not lower than 20 km below the end height. These criteria were empirically determined from all-sky meteor observations. They are meant to reject non-meteor events (such as coincident cloud triggers on multiple stations) and are not more stringent so as to avoid throwing out valid meteors that might appear invalid due to bad astrometric centroid picks. Based on the written summary table, each station automatically copies the raw video frame data for valid events to a local shuttle disk for archival purposes, but can also be configured to copy via the internet.

Shower associations are made using the IAU Meteor Data Center catalogue (<http://www.astro.amu.edu.pl/jopek/MDC2007/>) with geocentric radiant agreement of  $7.5^\circ$  and geocentric speed agree-

ment of 20%. The trajectory solutions are used to convert the apparent magnitudes to their absolute magnitude equivalents at 100 km range. For our Gen-III bandpass, Weryk and Brown (2013) showed that for a 4500K blackbody spectrum, absolute meteor magnitude ( $M$ ) calibrated to stellar  $R$ -band relates to photon radiant power ( $I$ , in units of watts) according to:

$$M = 7.285 - 2.5 \log_{10} I \quad (4)$$

The log-sum-pixel magnitudes are integrated for each station, and the station with the largest integral is taken to be the best representative for that event. This chosen light curve is likely the highest SNR and/or is more complete, meaning more of the trail was visible in the FOV. The calibrated light curve for this station in absolute magnitude units is interpolated using a cubic spline function and integrated to give an ablated mass estimate using the luminous efficiency of Weryk and Brown (2013). Because the event may have started and/or ended outside the FOV, the mass represents a lower limit.

## 4. Results

Here we present a selection of example events captured by the guided system to demonstrate the capability of CAMO.

### 4.1. Meteor phenomenology

Fig. 4 shows a composite of one frame extracted from the narrow-field camera for each of 18 separate events, illustrating differences in the phenomenological structure of meteors at metre scale and at  $\sim 10$  ms resolution. Fragmentation on this scale cannot be resolved by the wide-field camera, but is very commonly observed by the narrow-field camera. Qualitatively, the meteor trail radius varies widely between events, although in absolute terms it is dependent on the range to each meteor.

### 4.2. Discrete meteoroid fragmentation

Fig. 5 shows frame snapshots of meteor 20120824\_081141 (i.e. occurring at 08:11:41 UTC on August 24, 2012), spaced every four frames (50 ms), as tracked by the narrow-field camera. This illustrates the time-dependent fragmentation morphology, where individual fragments are visible along the meteor trail. We find 17% of all well-tracked meteors display one or more clear fragments. Approximately 75% of all meteors show either discrete fragments

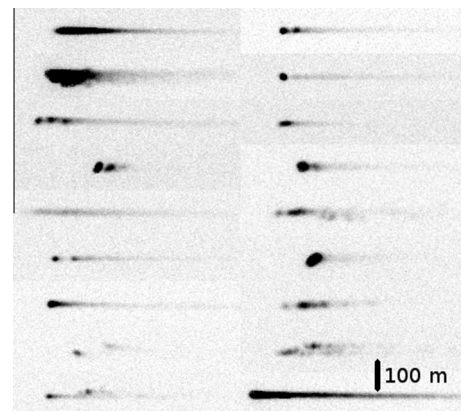
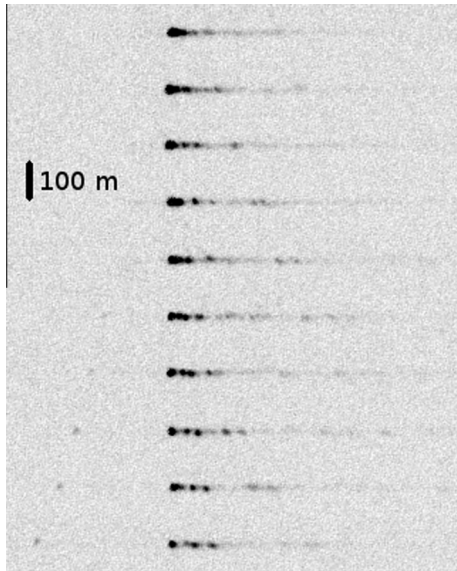


Fig. 4. A composite of 18 separate meteors showing different structure of the meteor during ablation. The 100 m distance scale is shown for an average range of 130 km.



**Fig. 5.** An example tracked meteor (20120824\_081141) recorded by the narrow-field guided camera, centred on the largest fragment. Snapshots are spaced by four frames (50 ms), with time increasing top to bottom. Multiple pieces quickly become separated. The 100 m distance scale is shown for an average range of 130 km.

**Table 3**

Event 20120826\_075833, detected by both CMOR and CAMO. The radar and video derived velocity solutions are shown, along with the CAMO data reduced manually (by methods of Weryk and Brown, 2012, 2013) to illustrate differences between automatic and manual solutions. The local radiant is given by  $\eta$ , the zenith angle, and  $\rho$ , the azimuth angle measured North of East. For the CAMO solutions, the specular height  $H_S$  was computed from the frame closest to  $90^\circ$  from the radiant (i.e. at the echo specular point).

	CMOR (user)	CAMO (auto)	CAMO (user)
$v_p$ (km/s)	42.48	$39.24 \pm 0.52$	$39.15 \pm 0.19$
$H_B$ (km)	?	$102.83 \pm 0.06$	$103.82 \pm 0.04$
$H_S$ (km)	95.69	96.63	97.41
$H_E$ (km)	?	$95.32 \pm 0.07$	$92.94 \pm 0.04$
$\eta$ ( $^\circ$ )	51.45	$51.59 \pm 0.84$	$52.17 \pm 0.32$
$\rho$ ( $^\circ$ )	$-105.75$	$-105.90 \pm 0.28$	$-105.48 \pm 0.11$

or significant wake, emphasising the dominant role of fragmentation in meteor ablation at these mass and size scales.

#### 4.3. Simultaneous radar-video meteor observations

Due to the nature of specular scattering in radar meteor trails, simultaneous radar-video detections are rare, accounting for  $\sim 5\%$  of all meteors (Weryk and Brown, 2012). These observations however, can be used to constrain  $\tau_l$ , the luminous efficiency (Weryk and Brown, 2013). We present here a sample detection, analysed using the methods of Weryk and Brown (2012, 2013).

Table 3 shows the trajectory solution for meteor 20120826\_075833, detected simultaneously by CAMO and CMOR. This Southern  $\delta$ -Aquiriid (SDA) meteor was observed by the radar towards the end of its corresponding video light curve. In terms of minimum spatial distance, the video meteor location from CAMO was 0.020 s (1.6 frames) later,  $0.70^\circ$  away from the radar specular point/time. In terms of minimum temporal separation, the closest video frame was 0.005 s (0.4 frames) before, at which time the meteor was  $0.78^\circ$  away from the interferometrically determined echo specular point. This is consistent with the  $\sim 0.8^\circ$  radar interferometry accuracy found by Weryk and Brown (2013). Because the CAMO and CMOR timebases are both NTP calibrated, we expect

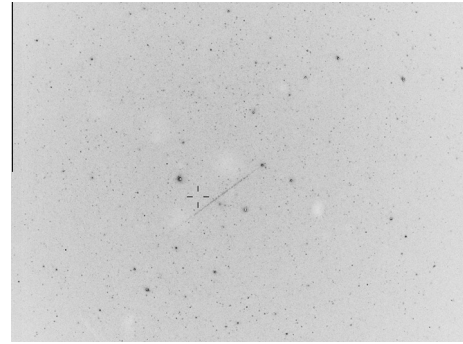


**Fig. 6.** Composite wide-field camera stack for event 20120826\_075833, shown for Tavistock. The location of the echo specular point as measured by CMOR is shown by the cross-hairs and occurs near the end of the video light curve. The meteor travels towards the lower left.

the location of the video meteor at the time of the echo to be better correlated with the radar specular point, which is illustrated in Fig. 6. The spatial point represents the minimum angular distance to the trail. In this example, the radar echo peaked at an absolute receiver power of  $-86.5$  dBm, corresponding to an electron line density of  $q = 3.3 \times 10^{14} \text{ e}^-/\text{m}$  which is a transition type echo. Using the definition of radio magnitude from Weryk and Brown (2013), this corresponds to  $+2.4^M$  in the Gen-III bandpass, similar to the automatically determined absolute magnitude of  $+2.8^M$  measured by CAMO with the ASGAR software. Fig. 7 shows a comparison between the automatic and manual light curves for the Tavistock station. Also shown is the radio-magnitude for the radar specular point. The automatic light curve has a smaller time span than the manually measured light curve, due to the lower detection sensitivity of the ASGAR configuration.

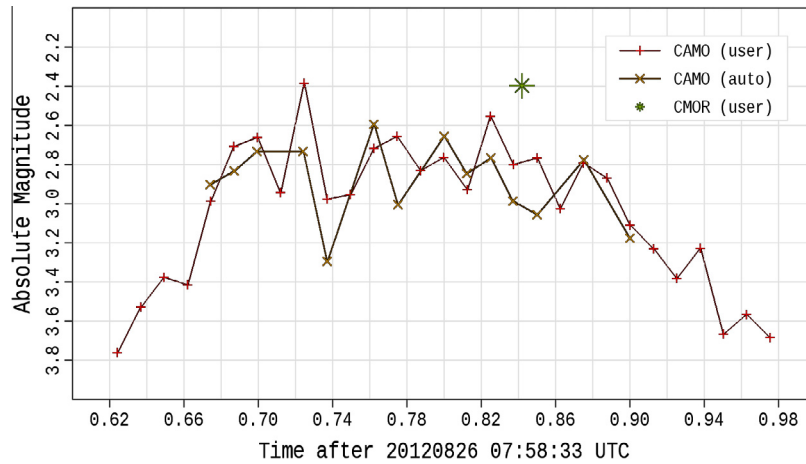
#### 4.4. Higher precision deceleration

Table 4 shows the trajectory solution for event 20120824\_074752, a Southern  $\delta$ -Aquiriid analysed automatically by ASGAR using the wide field data, and manually with the wide and narrow field data. The narrow field centroids were mapped to their corresponding zenith and azimuth angles by bootstrapping to the wide field camera, a process where the narrow-field pixel position measurements were converted into the equivalent 16-bit hardware mirror encoder values that would position the meteor in the centre of the FOV. These mirror encoder positions were then reversed mapped through the guide plate to their equivalent wide field pixel locations, and then converted to local zenith and azimuth angles using the wide field plate calibration. This limits our narrow-field meteor centroid accuracy to the equivalent stellar centroid accuracy in the wide-field camera, though our precision is limited by the pixel scale of the narrow-field camera.

Fig. 8 shows the trajectory fit residuals perpendicular to the direction of motion for the user determined wide-field and narrow-field solutions. While the wide field has residuals with a standard deviation of many tens of metres, the narrow-field is consistently around one metre. However, these fit residuals represent the minimum transverse spread of each sight-line from the meteor trajectory. In order to estimate the precision along the meteor trail, we compute the trail offset:

$$\Delta L = L - v_p t \quad (5)$$

Where  $t$  is the relative time of a centroid pick for a given frame, and  $L$  is the length along the trail. For meteors that show no deceleration,  $\Delta L = 0$  for all points along the trail. With deceleration, a plot of  $\Delta L$  vs  $H$  will not be constant. The scatter in  $\Delta L$  vs  $H$  provides a



**Fig. 7.** Light curve for event 20120826\_075833, shown for the Tavistock CAMO station. The light curves shown are the automated ASGARD light curve, a manually (user) processed light curve, and the equivalent radio-magnitude recorded by CMOR plotted at the time of peak received echo power. Because CMOR is a specular backscatter radar, its radio magnitude represents a single value on the light curve. Uncertainties at +2.6<sup>M</sup> are roughly 0.04<sup>M</sup> for counting statistics alone. Impulsive shot-noise error will contribute more error.

**Table 4**

The trajectory solution for event 20120824\_074752 analysed automatically and manually. The narrow-field solution has a lower start height due to track latency, and a lower end height due to being more sensitive than the wide-field camera. It is also seen that a manually reduced solution has higher accuracy than the automatically determined solution, while the narrow-field solution has higher precision.

	Wide (auto)	Wide (user)	Narr (user)
$v_p$ (km/s)	$38.20 \pm 0.06$	$38.21 \pm 0.21$	$37.48 \pm 0.13$
$H_B$ (km)	$99.178 \pm 0.042$	$101.150 \pm 0.024$	$95.143 \pm 0.002$
$H_E$ (km)	$86.048 \pm 0.056$	$85.218 \pm 0.026$	$83.604 \pm 0.002$
$\eta$ (°)	$51.299 \pm 0.360$	$51.356 \pm 0.149$	$51.346 \pm 0.013$
$\rho$ (°)	$-101.634 \pm 0.092$	$-101.708 \pm 0.042$	$-101.919 \pm 0.004$

direct estimate of the along-the-track measurement precision. For our example meteor, we plot the trail offset for all cameras in Fig. 9. The higher precision of centroids along the meteor trail in the narrow-field solution is evident from the low point-to-point scatter. From this solution, it is seen that deceleration is present along most of the trajectory, and is on a scale not resolvable by the wide-field camera.

For this meteor, a fit of  $L$  vs  $t$  for 12 points near the start of the narrow-field trajectory gave a speed of  $37.919 \pm 0.052$  km/s for

Tavistock, and  $37.995 \pm 0.140$  km/s for Elginfield. These represent 0.1% and 0.4% precisions, respectively. We note that the out-of-atmosphere speed uncertainty is driven entirely by the uncertain correction of the small loss in speed in the earliest (unobserved) part of the meteor trail. For rare events where the narrow-field is able to begin tracking at higher heights (>115 km), we therefore expect the ultimate accuracy of direct speed measurements to never be better than a few tenths of a percent.

#### 4.5. Meteor shower studies: the Orionids

Meteor showers present an opportunity to study meteoroids that are related, and in some cases have known parent bodies. Figs. 10 and 11 show 66 automatically detected and analysed meteors from the 2010 and 2011 Orionid meteor shower. Kresák and Porubčan (1970) used high-precision photographic meteors to determine the physical radiant spread of many showers. For 80 Orionid meteors, they found a mean radiant spread of  $0.84^\circ$ . As our spread in geocentric declination alone is  $\delta_g = 15.8^\circ \pm 2.9^\circ$ , this suggests that the radiant spread of our meteors as measured automatically by the wide-field camera of the guided system is dominated by measurement error. The error bars for individual

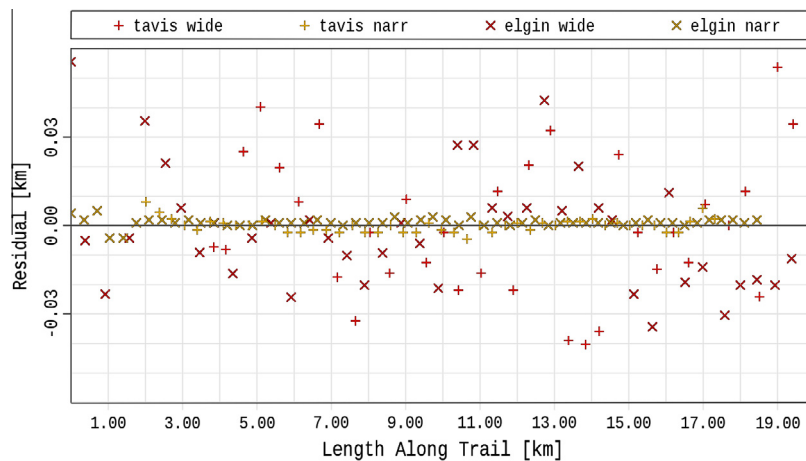


**Fig. 8.** Transverse residuals between the centroid sight lines and the best fit meteor trajectory. The narrow-field solution shows a standard deviation of one metre, an order of magnitude more precise than the wide-field solution. Note that the length scales are relative to the start of the meteor as observed by each method. The narrow-field solution begins 2 km along the wide-field solution.

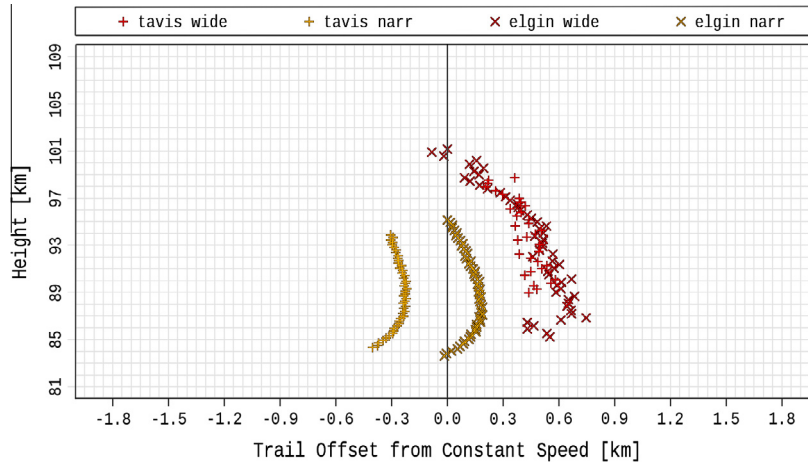


**Fig. 9.** Trail offset for event 20120824\_074752, showing obvious deceleration with the narrow-field camera. The lower scatter between individual frames shows the improved precision of guided meteors measured in the narrow-field camera compared to the wide-field camera. All data were manually reduced. The absolute trail offsets represent timing differences between systems. These have been left as measured to provide offsets between cameras to allow easier viewing of data from each station.

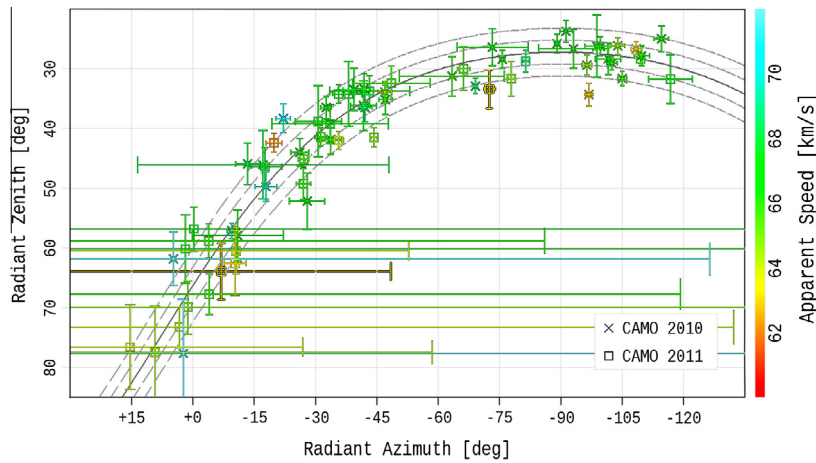


**Fig. 10.** Individual radiants from Tavistock of the Orionid meteor shower from 2010 and 2011. They are plotted as local zenith and azimuth (North of East) angles as determined from the wide-field camera of the guided system. The error bars were determined from Monte-Carlo modelling as described in the text. The curved lines represent declinations spaced 2°, centred at  $\delta_p = 16^\circ$ .

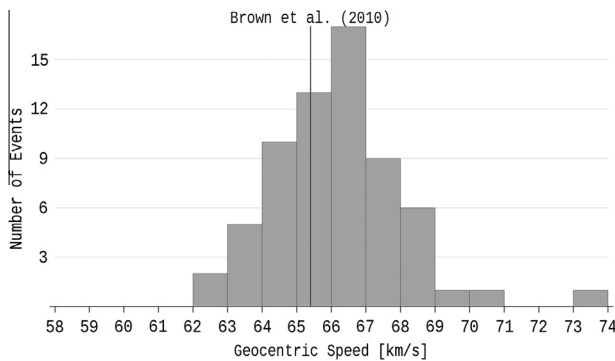


**Fig. 11.** The geocentric speed distribution of the automatically detected and analysed Orionid meteors from 2010 and 2011 based on the wide-field camera. Also shown is the expected geocentric speed from the Brown et al. (2010a) radar shower catalogue. Individual speed uncertainties are 3% on average.

events in Fig. 10 were determined by Monte-Carlo modelling as described by Weryk and Brown (2012) assuming a random pixel error of 2.0 pixels, resulting in a radiant spread with a standard deviation of 3.7°. Decreasing the random error to 1.5 pixels gives a radiant

spread with a standard deviation of 2.7°. This suggests our centroid picks are accurate to  $\sim 2$  pixels assuming all our radiant spread is due to measurement error. Our radiant scatter is comparable to SonotaCo (2009), who required an average spread of 5° for shower association.

Meteors with a zenith entry angle  $\eta > 55^\circ$  had radiants from the East. This is along the line connecting our two stations, resulting in poor convergence angles. More deceleration in radar detected events is likely why our speed distribution (Fig. 11) is skewed to higher speed than given by Brown et al. (2010) as that study used specular radar echoes at lower heights where larger deceleration is expected to occur. Fig. 12 shows the 51 Orionids with  $\eta < 55^\circ$  in Sun-centred ecliptic coordinates precessed to the J2000 epoch. Also shown is the radiant location from the Brown et al. (2010) catalogue for solar longitude  $\lambda = 198\text{--}226^\circ$ .

## 5. Conclusions and future work

The CAMO system has been developed to automatically record and analyse video meteors, and has been operating automatically at two stations since 2009. The primary goals of CAMO are to ac-

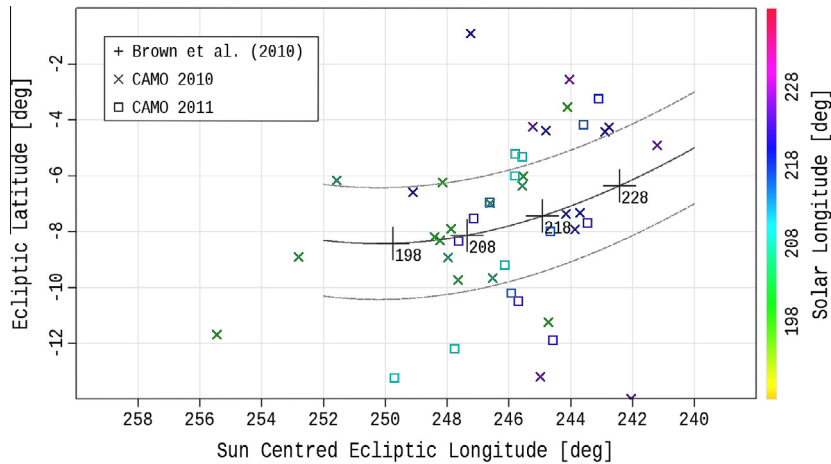


**Fig. 12.** Individual geocentric radiant (precessed to J2000) of the Orionid meteor shower from 2010 and 2011, plotted in ecliptic latitude and Sun centred ecliptic longitude. Also shown is the expected radiant from the Brown et al. (2010) catalogue for different solar longitudes. Events were associated with the Orionid stream if they were  $<7.5^\circ$  from the Brown et al. (2010) radiant.

quire meteor observations to help constrain numerical ablation models, and to measure the meteoroid mass influx at the Earth.

We presented example meteor detections to demonstrate the capability of our system. Discrete meteoroid fragmentation was noted in 17% of cases, while meteor wake was present in more than half of our observed meteors. We demonstrated that CAMO is capable of observing simultaneous radar-video meteors with CMOR, which will allow for comparisons between radar ionisation and video radiant power to place constraints on the luminous efficiency in our Gen-III intensified bandpass. Our automatic wide-field camera solutions have average radiant errors of  $\sim 3^\circ$  and speed uncertainties of 3%. Our manually determined narrow-field trajectory solutions have precisions in speed of a few tenths of a percent, and radiant precisions of  $\sim 0.01^\circ$ .

In future papers, we will discuss further examples of meteoroid fragmentation, measure meteor trail radii important for constraining the initial trail radii of radar meteors, and discuss stream specific estimates of the luminous efficiency,  $\tau_l$ .

## Acknowledgments

The authors thank the Canada Foundation of Innovation and the NASA Meteoroid Environment Office (MEO) for funding support (NASA Cooperative Agreement NNX11AB76A), and also thank Pete Gural and Bob Hawkes for helpful discussions. Jiri Borovička kindly provided the MILIG video trajectory solver program. RJW thanks the three anonymous referees for their helpful comments.

## References

Borovička, J., 1990. The comparison of two methods of determining meteor trajectories from photographs. *Bull. Astron. Inst. Czech.* 41, 391–396.  
 Brown, P., Weryk, R.J., Kohut, S., Edwards, W.N., Krzeminski, Z., 2010a. Development of an all-sky video meteor network in southern Ontario, Canada. *The ASGARD system*. *WGN, J. Int. Meteor. Org.* 38, 25–30.

Brown, P., Wong, D.K., Weryk, R.J., Wiegert, P., 2010b. A meteoroid stream survey using the Canadian Meteor Orbit Radar. II: Identification of minor showers using a 3D wavelet transform. *Icarus* 207, 66–81.  
 Brownlee, D., Joswiak, D., Graciela, M., 2012. Overview of the rocky component of Wild 2 comet samples: Insight into the early Solar System, relationship with meteoritic materials and the differences between comets and asteroids. *Meteorit. Planet. Sci.* 47, 453–470.  
 Cambridge Technology, 2012. The Moving Coil Galvanometer Family – Model 6900. <<http://www.camtech.com/products/6450/6900.html>> (accessed 17.08.12).  
 Gural, P.S., 1997. An operational autonomous meteor detector: Development issues and early results. *WGN, J. Int. Meteor. Org.* 25, 136–140.  
 Gural, P.S., Jenniskens, P.M., Varros, G., 2004. Results from the AIM-IT meteor tracking system. *Earth Moon Planets* 95, 541–552.  
 Hawkes, R.L., 2002. Detection and analysis procedures for visual, photographic and image intensified CCD meteor observations. In: *Meteors in the Earth's Atmosphere*. Cambridge University Press.  
 Jenniskens, P., Gural, P., Varros, G., Stenbaek-Nielsen, 2004. AIM-IT: Rapid pointing to meteors in airborne observations. In: *Proceedings SOFIA Upper Deck Science Opportunities Workshop*, NASA Ames Research Center, June 22–23, 2004, pp. 58–60.  
 Jones, J., Campbell-Brown, M., 2005. The initial train radius of sporadic meteors. *Mon. Not. R. Astron. Soc.* 359, 1131–1136.  
 Jones, J. et al., 2005. The Canadian Meteor Orbit Radar: System overview and preliminary results. *Planet. Space Sci.* 53, 413–421.  
 Kresák, L., Porubčan, V., 1970. The dispersion of meteors in meteor streams. I. The size of the radiant areas. *Bull. Astron. Inst. Czech.* 21, 153–169.  
 Molau, S., 1999. The meteor detection software MetRec. In: *Proceedings of the International Meteor Conference 1998*, Stará Lesná, Slovakia, pp. 9–16.  
 Musci, R., Weryk, R.J., Brown, P., Campbell-Brown, M.D., Wiegert, P.A., 2012. An optical survey for millimeter-sized interstellar meteoroids. *Astrophys. J.* 745, 161–166.  
 Myers, J.R., Sande, C.B., Miller, A.C., Warren Jr., W.H., Tracowell, D.A., 2002. SKY2000 Master Catalog, Version 4. Goddard Space Flight Center, Flight Dynamics Division, V/109.  
 SonotaCo.com.: UFOCapture, Software for Unknown Universe. <[http://www.sonotaco.com/e\\_index.html](http://www.sonotaco.com/e_index.html)> (accessed 26.08.12).  
 Weryk, R.J., Brown, P.G., 2012. Simultaneous radar and video meteors – I: Metric comparisons. *Planet. Space Sci.* 62, 132–152.  
 Weryk, R.J., Brown, P.G., 2013. Simultaneous radar and video meteors – II: Photometry and ionisation. *Planet. Space Sci.* 81, 32–47.  
 Weryk, R.J. et al., 2008. The southern Ontario all-sky meteor camera network. *Earth Moon Planets* 102, 241–246.